Numerical simulation of electroosmotic flow in a rectangular microchannel with use of magnetic and electric fields

Mohsen Saghafian[a,*], Hossein Seyedzadeh[a], and Abolfazl Moradmand[a]

a. Department of Mechanical Engineering, Isfahan University of Technology, Isfahan, 8415683111, Iran

Abstract

Pumping fluid is one of the crucial parts of any microfluidic system. Using electric and magnetic fields as a substitute for moving parts can have many advantages. In this study hydrodynamic and heat transfer characteristics of electroosmotic flow under influence of lateral electric and transverse magnetic field, are studied numerically. Results indicate that the dimensionless parameters such as Hartmann number, intensity of the lateral electric field, pressure gradient parameter and aspect ratio have an important role in controlling flow. It can be implied that the enhancement of pressure gradient leads to the decrease of critical Hartmann number, and this dependency can be reduced from 44% to 7% for $S = 0.5$ to $S = 50$ in two pressure gradients of $\Omega = 1$ and $\Omega = 20$. In addition, the reduction of aspect ratio of microchannel section leads to the increment of critical Hartmann number in a specified lateral electric field. At the end, thermal analysis is being done by consideration of the effects of magnetic and electric fields on the Nusselt number.

1   Introduction

Microfluidics and micro-electro-mechanical systems (MEMS) have various applications such as heat exchangers, micro-pumps, separation machines, etc. [1–3]. The flow pumping part has been especially considered due to flow transfers to the different parts of fluidic system. In general, micro-pumps are divided into mechanical and non-mechanical groups. Due to the complexities of construction of moving parts and high pressure drop in the micro scale, mechanical fluid transfer is being involved with limitations, hence, transport mechanism has been used without moving parts [4]. There are different methods to transfer fluid inside the narrow channels such as applying pressure gradients, capillary effect and electric or magnetic fields [5–7]. Therefore, in recent decades, researchers have shown the potential of using the combination of electrokinetic and magnetohydrodynamics in order to achieve the ideal flow control in devices with different shapes. Due to mechanical pumping issues in engineering applications such high power requirements, friction loss, etc., the aforementioned techniques are crucial for stimulating fluids in modern industries. In the meantime, fluid flow and heat transfer are considered in the narrow channels.

Transport phenomenon has distinctive characteristics in the micro scale compared to macro scale which is due to the surface effects such as electric double layer (EDL) [8]. The electric double layer is created due to the interaction of the ionized solution with free charge on the dielectric surfaces. Due to the electric field, mobile ions move in the EDL regions leading to

42 transport of bulk liquid with viscose effects. This concept is called electroosmotic flow (EOF)
43 [9]. Jung and Lee [4] were the first researchers who investigated micro pumps by using the
44 driving force of MHD flow (Lorentz force), analytically and experimentally. They reported the
45 amount of pressure difference and flow rate in a special condition. Wang et al. [10] numerically
46 simulated 2-D, laminar and fully developed magnetohydrodynamic (MHD) flow inside a
47 microchannel. They added Lorentz force as a source term to the momentum equation instead of
48 analytical solution of Lorentz force due to applied magnetic field in momentum equation. Also,
49 they revealed that induced Lorentz force has a significant effect on the flow velocity profile.
50 Chakraborty and Paul [11] implemented electromagnetohydrodynamic (EMHD) flow by
51 considering pressure gradient inside a 2-D microchannel. They indicated that in the presence of
52 specified lateral electric field with the aid of a relatively low-power magnetic field, the
53 volumetric flow rate enhances. However, for high-intensity magnetic field and in the presence of
54 lateral electric field, the volumetric flow rate decreases. Duwairi and Abdullah [12] studied heat
55 transfer and MHD flow inside a rectangular micro-pump. They obtained velocity and
56 temperature distribution analytically and numerically, then investigated the effects of different
57 parameters on them. Chakraborty et al. [13] investigated heat transfer characteristics of a
58 thermally fully developed EMHD flow between two parallel plates. They revealed that for a
59 specific pressure gradient and axial electric field, the heat transfer characteristics in the micro
60 scale can be significantly controlled by changing lateral electric and magnetic fields. Scandon et
61 al. [14] analytically studied hydrodynamic and heat transfer characteristics of an EMHD and
62 pressure-driven flow of a viscoelastic fluid inside a rectangular microchannel. Their results
63 demonstrated that the volumetric flow rate enhances in the presence of electric and magnetic
64 fields and also, this increment gives rise to the pressure gradient. In addition, the volumetric flow
65 rate of Newtonian fluids is more sensitive to the MHD forces compared to viscoelastic fluids.
66 Kiasatfar and Pourmahmoud [15] investigated flow and heat transfer of non-Newtonian
67 conductive fluid inside a square microchannel under influence of a uniform magnetic field by
68 using finite difference method. The obtained results revealed that increase in Hartmann number
69 leads to a decrease in the maximum velocity of fluid and also, leads to the velocity profile's
70 uniformity. Wang et al. [16] investigated EMHD flow of a non-Newtonian fluid between two
71 parallel micro plates analytically and numerically by using perturbation techniques and
72 compared the results with each other. They found out that by increasing Hartmann number,
73 velocity and temperature decrease due to applied Lorentz force. Also, the augmentation of
74 electric field intensity leads to the enhancement of velocity and temperature distributions in a
75 specified Hartmann number. Sarkar et al. [9] studied the effect of non-uniform magnetic field on
76 the mixed electroosmotic pressure-driven flow for thermally developed flow inside a fluidic
77 narrow channel. They investigated flow, heat transfer and entropy generation and indicated that
78 velocity and temperature distributions are symmetric when Hartmann number is non-zero. Qi
79 and Wu [17] analytically implemented EMHD flow inside a rectangular microchannel under
80 influence of the simultaneous magnetic and electric fields and obtained electric potential
81 distribution. Also, they positioned the electric field as the deviant from the microchannel axis.
82 Young et al. [18] investigated fluid flow and heat transfer of electroosmotic flow with the MHD
83 effects inside a rectangular microchannel. They figured out that lateral electric field has a
84 significant effect on the flow control and heat transfer and without the effect of lateral field, the
85 normal velocity decreases gradually by increasing Hartmann number due to magnetic field's
86 deterrent force. Moradmand et al. [19] numerically implemented Newtonian fluid's flow
87 between two parallel micro plates, influenced by electric and magnetic fields. They concluded

88 that in the electroosmotic flow, applying lateral electric field and transverse magnetic field
89 causes creation of maximum possible flow rate for each Hartmann number and consequently, the
90 increment of Hartmann number leads to reduction in flow velocity. Yang and Jian [20] studied a
91 fully developed EMHD flow through the microchannel analytically and numerically. They used
92 slip patterned boundary conditions with perturbation techniques under the assumption of small
93 Reynolds number for analytical solution, and finite-difference method for numerical solution.
94 Their results show that patterned slippage over the microchannel walls will induce a transverse
95 flow which augments the mixing rate. Deng and Wu [21] investigated the electroosmotic and
96 pressure-driven flow of power-law fluids in a circular microchannel. The results show that both
97 the viscosity and electroosmotic characters of inner power-law fluid, and the peripheral power-
98 law fluid can affect the inner flow. Ge et al [22] investigated the thermal resistance and pressure
99 drop for the combination of Micro/mini-channel heat sinks, with rectangular rib, by the multi-
100 objective genetic algorithm and particle swarm optimization. Their results indicated that rib
101 increases flow area, which results in transporting coolant flow in the secondary flow and
102 consequently, heat transfer increment. Moreover, by changing shape from rectangular cross-
103 section to curvy, pumping power reduced. Wang et al [23] studied the flow mechanism and heat
104 transfer increment of microchannel heat sinks with bi-direction ribs, numerically, and
105 experimentally. Their results indicated that this design has better heat transfer, which is being
106 concluded by significantly better Nusselt numbers. Biswas et al [24] studied the thermal
107 efficiency of a hybrid nano-fluid (Cu–Al_2O_3–H_2O) flow inside a porous oblique wavy cavity,
108 with use of partly active magnetic field. Their results indicate that partially applied magnetic
109 field on a complex wavy surface increase heat transfer significantly than the entire magnetic
110 field. Mandal et al [25] numerically studied the thermo-fluidic transport of a magnetic
111 hydrodynamic mixture, including nanofluid, in a cavity with a wavy wall. They also used an
112 artificial neural network (ANN) method for statistical data. They considered the parameters
113 influencing the flow for thermal evaluation. Their results revealed that heat transfer rate will
114 increase for the curved-shape geometries. Moreover, they stated that ANN method can make an
115 exact prediction for complicated shapes and Multiphysics geometries. Datta et al [26]
116 investigated heat transfer enhancement by studying three-dimensional transient conjugate heat
117 transfer in microchannel heat sinks. They implemented different flow structures like
118 combinations of ribs, cavities and protrusions on the side walls of a microchannel, and they used
119 various geometric parameters like sidewall angles, number, and height of the top. Their results
120 indicated that by changing the geometric parameters, they can control the heat transfer with
121 them. Amit et al [27] numerically studied the conjugate heat transfer for disruptive structures
122 placed symmetrically in a rectangular microchannel. They used structures such as Triangular
123 cavity, Secondary branch and Blockage to design a microsink. Their results indicate that cavity
124 with secondary branch and blockage structure has the highest thermal performance and lowest
125 entropy generation. So, the secondary branch can improve thermal performance of a
126 microchannel with rectangular cavity. Biswas et al [28] studied the free aspiration technique for
127 heat transfer increment on MHD thermal convection and porous substances, by solving coupled
128 mathematical equations of continuity, momentum, and energy. They used Maxwell model to
129 utilize magnetic field and Brinkman-Forcheimer-Darcy model for porous media. Their results
130 show that the free aspiration technique is able to remove heat from heat sources of the cavities,
131 so it can increase heat transfer with no external pumping method. EMHD flow can be used in the
132 bioconvection micropolar nanofluid, which is investigated in the work of Alharbi et al [29]. The

3

133   results of their work indicated the heat transfer rate of nanofluid, with use of self-similar
134   variables. They also indicated that these parameters could control the flow and heat transfer.

135   Micropumps have many applications, especially in medicine delivery systems. One of the
136   real applications of the current research's micropump is mentioned in the work of Ciocanel et al
137   [30], which they manufactured an integrated EMHD micropump, which is a flow channel
138   containing fluid to be pumped. They used electrodes and magnets to be responsible for electric
139   and magnetic fields, which pump the fluid by a combination of electroosmotic and MHD flow.
140   Also, this study has potential applications in biomedical devices. One specific real problem
141   involving electroosmotic flow with magnetic and electric fields is the development of
142   microfluidic devices for biomedical applications, such as cell separation, manipulation in
143   microfluidics, and drug delivery. For example, in a study published in the journal of magnetism
144   and magnetic materials in 2021, researchers investigated the use of a magnetophoretic
145   microfluidic chip with use of electroosmotic flow, to separate magnetic particles (MPs) from
146   human blood. Applying the magnetic field and electric potential makes a perfect on-chip
147   separation, which is versatile for targeting magnetic particles [31].

148   Following a detailed review of the literature, many previous results pertain to 2D problems.
149   But for practical applications, like drug targeting, cancer tumor treatment, devices for cell
150   separation, endoscopy, and adjusting blood flow during surgery, it is imperative to provide a 3D
151   solution. Moreover, to the best of our knowledge, the effect of the microchannel's geometry on
152   the flow and critical Hartmann number has not been performed so far. Thus, the impact of
153   microchannel geometry on the fluid flow and critical Hartmann number is investigated by
154   considering different aspect ratios ($a = H/W = 0$, 0.2, 0.5, 1, 2). To model the electric potential
155   distribution in the vicinity of walls, Poisson-Boltzmann equations with the linear Debye-Hückel
156   approximation is used. The governing equations are discretized by applying the finite volume
157   method and solved using a numerical code. In addition, for exact modeling, Joule heating is
158   considered in the energy equation. The essential hydrodynamic and heat transfer parameters such
159   as critical Hartmann number and Nusselt number are determined. The effect of different
160   variables such as aspect ratio, the intensity of electric and magnetic fields on flow is studied.

161

162 **2   Problem description**

163   In the current research, fluid flow is studied inside a rectangular microchannel with the height
164   of *2H*, width of *2W* and length of *L* (according to Figure 1). The uniform axial and lateral
165   electric fields (E_x and E_z) are applied along the *x* and *z* axes and also, the uniform transverse
166   magnetic field (B_y) is applied along the *y* axis of microchannel. The coordinate axes are
167   positioned such that the *x* axis is along the microchannel axis and there is the axial pressure
168   gradient along it. The surface of microchannel is a dielectric surface when exposed to an
169   electrolyte fluid, forms a layer called electric double layer (EDL). The Poisson-Boltzmann
170   equation is used for modeling the ions in EDL.

171

3 Mathematical modeling

3-1 Electrokinetic equations

174 The charged walls of the channel create EDL in the vicinity of wall when exposed to the
175 electrolyte solution. The electric potential distribution can be obtained by using Poisson equation
176 [32]:

$$\nabla^2 \psi = -\frac{\rho_e}{\varepsilon\varepsilon_0} \tag{1}$$

177 When ε_0 is the permittivity of free space and ε_0 is the dielectric constant of electrolyte solution.

178 The electric charge density ρ_e for symmetric electrolyte solution $z_+ = -z_-$ is [32]:

$$\rho_e = -2zen_0 \sinh\left(\frac{ze\psi}{k_BT}\right) \tag{2}$$

179 By combining Equations (1) and (2), the linearized Poisson-Boltzmann equation is obtained by
180 applying Debye-Hückel approximation [32]:

$$\nabla^2 \psi = \kappa^2 \psi \tag{3}$$

181 Consequently, by using Eq. (3), ψ is obtained and then by using obtained ψ and Poisson
182 equation (Eq. (1)), ρ_e will be determined. Now, by computing electric charge density, the
183 volumetric electrokinetic force or the force due to the electric field applied to fluid
184 (electroosmotic force), can be obtained [32]:

$$\overrightarrow{F_{EK}} = \rho_e \vec{E} \tag{4}$$

3-2 Magnetohydrodynamic equations

186 The force due to magnetic field (Lorentz force) is described as [33]:

$$\overrightarrow{F_B} = \vec{J} \times \vec{B} \tag{5}$$

187 Magnetic field $\vec{B}$ includes an applied external field $\vec{B}_0$ and an inducted field $\vec{b}$. In micro scale
188 flows, due to the low characteristic length and low average velocity, magnetic Reynolds number
189 is low and consequently, the effect of induced magnetic field can be neglected against the
190 applied external magnetic field. As a result, total magnetic field can be estimated by externally
191 applied magnetic field [32,34]. J is induced electric current density [33]:

$$\vec{J} = \sigma\left(\vec{E} + \vec{U} \times \vec{B}\right) \tag{6}$$

3-3 Flow and energy equations under influence of electric and magnetic fields

193 According to the mentioned contents, volumetric force due to electric and magnetic fields is
194 as follows [11]:

$$\vec{F} = \overrightarrow{F_{EK}} + \overrightarrow{F_B} = \rho_e \vec{E} + \vec{J} \times \vec{B} \tag{7}$$

5

195 The assumptions considered are Newtonian fluid, steady state and incompressible flow. Also,
196 pressure gradient is considered along the channel length. Heat flux is constantly applied to the
197 side walls (up, down, right, left). Moreover, joule heating term is applied in the energy equation
198 and viscous dissipation term is neglected. Therefore, the governing equations are as the
199 following [13]:

$$\nabla.\vec{V} = 0 \tag{8}$$

$$\rho_f\left(\left(\vec{V}.\nabla\right)\vec{V}\right) = -\nabla P + \mu\nabla^2\vec{V} + \vec{F} \tag{9}$$

200 Where, $\vec{V} = u\hat{i} + v\hat{j} + w\hat{k}$, ρ_f, P, μ, and $\vec{B}$ are velocity field, fluid density, pressure, fluid
201 viscosity and volumetric force due to applied electric and magnetic fields on fluid, respectively.
202 By applying the resultant force as a source term, momentum equation components will be as
203 follows:

$$\rho_f\left(\left(\vec{V}.\nabla\right)u\right) = -\nabla P + \mu\nabla^2 u + \rho_e E_x - \sigma E_z B_y - \sigma u B_y^2 \tag{10}$$

$$\rho_f\left(\left(\vec{V}.\nabla\right)v\right) = -\nabla P + \mu\nabla^2 v \tag{11}$$

$$\rho_f\left(\left(\vec{V}.\nabla\right)w\right) = -\nabla P + \mu\nabla^2 w + \rho_e E_z + \sigma E_x B_y - \sigma w B_y^2 \tag{12}$$

204 Energy equation [18]:

$$\rho_f C_P\left(\left(\vec{V}.\nabla\right)T\right) = k\nabla^2 T \tag{13}$$

205 In Eq. (13), C_p is fluid's specific heat capacity in the constant pressure, T is temperature, k is
206 conductivity coefficient and S_j is the generated heat in the volume unit of fluid due to the
207 applied magnetic field to electrolyte solution (joule heating). By using Ohm's principle, joule
208 heating phenomenon can be modeled as the heat source [7]:

$$S_j = \frac{\vec{J}^2}{\sigma} \tag{14}$$

209 In Eq. (14), J and σ are electric current density and electrical conductivity of electrolyte solution,
210 respectively. Also, joule heating can be obtained by using the values of electric and magnetic
211 fields as follows:

$$S_j = \sigma\left[\left(\vec{E_x}^2 + \vec{E_z}^2\right) + \left(wB_y\right)^2 + \left(uB_y\right)^2 - 2wE_x B_y + 2uE_z B_y\right] \tag{15}$$

212 The boundary conditions of this study are presented in Table 1.

213

214 **4   Numerical Implementation**

215 A numerical code based on the finite volume method is developed to solve momentum and
216 energy equations (governing equations of fluid flow). The convection terms of governing
217 equations in the integral form are discretized by using the QUICK method on a collocated grid.

6

218 For pressure-velocity coupling, the pressure correction algorithm of SIMPLEC is applied. The
219 Rai-Chow method is used to prevent nonphysical oscillations of pressure and velocity.

220 After defining the physical properties of the system such as channel dimensions, properties of
221 the fluid, applied electric and magnetic fields and discretizing the domain, the following
222 procedures are applied for the present numerical simulation:

223 1) Solving the linearized Poisson-Boltzmann equation (Eq. (3)) to obtain electric potential
224 distribution and then calculate the electric charge density from Poisson Equation (Eq. (1))
225 2) Solving the Navier-Stokes equation using SIMPLEC algorithm (calculating and updating
226 the velocity field based on the fluid properties and the applied fields)
227 3) Solving energy equation considering constant heat flux and Joule heating
228 4) Iterating steps 1-3 until convergence

229 The convergence criterion is the residuals in the continuity. The algorithm continues iterating
230 until these criteria reach a desired level, such as when the residuals reduce by at least five orders
231 of magnitude to a small value (such as 10^{-5}). This indicates that the solution has converged to an
232 acceptable accuracy.

233 In this study, dimensionless parameters which are used for revealing the behavior of fluid are
234 presented in Table 2. The values of the non-dimensional parameters taken into account for the
235 following analysis reflect conditions that are practically realizable.

236 **5   Validation of numerical solving procedure**

237 **5-1   Investigation of mesh independency:**

238 In the present investigation, some channels with various geometries are investigated. For each
239 geometry, mesh independency is carried out separately in different values of electric and
240 magnetic fields. The related results of Poiseuille number and dimensionless temperature are
241 indicated in Table 3.

242 For a 3-D channel with a square cross-section, by increasing the grid from 40×40×100 to
243 80×80×200, the percentage of the change is less than 1%. Therefore, in this condition, a
244 40×40×100 grid is used as the primary grid for a microchannel with a square cross-section. For a
245 3-D microchannel with a rectangular cross-section, aspect ratios of $\square$ = 0.5 and $\square$ = 0.2 are
246 considered. According to what was mentioned about square microchannel, in this condition,
247 40×64×100 and 32×80×100 grids are regarded as the main grids. For a 2-D microchannel ($\square$ =
248 0), a 40×100 grid is proposed

249 **5-2   Validation**

250 Validation of numerical code is investigated for a 3-D microchannel with square cross-section
251 and 2-D microchannel, separately. To verify the accuracy of electric potential distribution in the
252 vicinity of wall in the electrolyte solution, the study of Mirbozorghi et al. [35] is used. According
253 to Figure 2 , dimensionless electric potential distribution of this study is in agreement with the
254 results of Mirbozorghi et al. with high accuracy. Also, this accordance is seen in the vicinity of
255 side wall region which has high potential variations.

256 For investigating the accuracy of numerical code of the fluid flow inside a square
257 microchannel influenced by a transverse magnetic field and pressure gradient, study of Kiasatfar

258 and Pourmahmood [15] is used. According to Figure 3, this investigation has good agreement
259 with the results of Kiasatfar and Pourmahmood with the error of 1.3%.

260   In order to investigate the accuracy of numerical code in a pure electroosmotic flow inside a
261 square microchannel, study of Deng et al. [36] is utilized. According to Figure 4 , for both values
262 of dimensionless parameters of Debye-Hückel ($\kappa = 20$ and $\kappa = 100$) in all cross-sections,
263 especially in the vicinity of wall, this research has acceptable concordance with that of Deng et al
264 [36]. Maximum difference is less than 1% in the case of $\kappa = 20$ and maximum variation is less
265 than 0.25% in the case of $\kappa = 100$. It should be noted that for nondimensionalization of this
266 profile, $U_0 = 0.001\ m/s$ is used [36]. Also, the effect of pressure gradient is not considered.

267   The study of Chakraborty et al. [13] is used for validation of a 2-D cross section
268 microchannel. According to Figure 5 , this research is in good accordance with the study of
269 Chakraborty et al. [13] in all cross sections of microchannel, especially in the vicinity of wall.

6   Results and discussions

271   In this section, the flow and thermal characteristics are discussed by means of the non-
272 dimensional parameters relevant to the present problem, which are presented in Table 2. The
273 used ranges for these non-dimensionalized numbers are $Ha \sim 0.1{:}10$, $S \sim 0{:}100$, $\Omega \sim 1{:}20$, $a \sim$
274 $0{:}2$, which fall into practical values[37,38]. The values for α and κ are being selected as 2256 and
275 20.

6-1   Hydrodynamic investigation

277 Figure 6 indicates developed velocity profile of fluid flow inside a square cross section
278 microchannel in the various values of Hartmann number (Ha) influenced by a dimensionless
279 axial electric field (α) and dimensionless pressure gradient (Ω), by neglecting lateral electric
280 field. As seen, by enhancing Ha, maximum velocity profile of passing flow decreases in
281 microchannel's section due to the deterrent effect of magnetic field on fluid flow. Also, the
282 simultaneous effects of deterrent force due to the transverse magnetic field and driving force due
283 to the axial electric field cause concussion in the velocity profile at the high values of Ha.

284   In the pure electroosmotic flow, the effect of axial electric field on microchannel leads to
285 apply electrokinetic force on fluid flow. Also, applying transverse magnetic field leads to a
286 reduction in maximum velocity in the microchannel's section. By affecting the lateral electric (
287 E_z) and transverse magnetic (B_y) fields, the primary electric field (E_x), and fluid flow along the
288 microchannel axis, secondary flow is created, seen by observing streamlines arrangement in
289 microchannel cross-section. Basically, lateral electric and transverse magnetic fields interact with
290 the charged particles in the fluid, inducing an electric current which generates a Lorentz force
291 perpendicular to the axial field and flow direction. This force causes the fluid to move in a
292 direction perpendicular to the primary flow. In Navier-Stokes equation along the z direction of
293 Eq. **Error! Reference source not found.**(12), three extra source terms ($\rho_e E_z$, $\sigma E_x B_y$ and $\sigma w B_y^2$
294) are responsible for secondary flow. According to drawn streamlines in the contours of V and W
295 velocity components of Figure 7, a flow is created opposite the Z-axis at the vicinity of walls
296 along the Z-axis. Also, by colliding with the lower wall of microchannel, it deviated inward ($Y =$
297 0). Eventually, it causes two rotational flows in the microchannel's section.

298 Figure 8 demonstrates dimensionless velocity profile of developed electroosmotic flow under
299 influence of axial and lateral electric fields, with pressure gradient inside a 3-D square
300 microchannel in different Hartmann numbers (*Ha*). By investigating the profiles, it can be
301 concluded that for *Ha* less than 2, *Ha* augmentation leads to velocity enhancement. While, in *Ha*
302 of greater than 2, increase in *Ha* results in velocity depletion. This phenomenon shows that if
303 lateral electric field is applied to a microchannel, increment of transverse magnetic field to a
304 specific value can increase maximum velocity in microchannel's section. After this particular
305 value, increment of *Ha* leads to a decrease in maximum velocity in microchannel. This specific
306 value is known as critical Hartmann number (Ha_{cr}) causing maximum flow rate in
307 microchannel. In this case, *Ha* of 2 is equal to the Ha_{cr} [19]. Critical Hartmann number depends
308 on the dimensionless parameter of lateral electric field (*S*). Therefore, its value can be obtained
309 in each value of *S*.

310   Figure 9 represents average velocity as the function of *Ha* for *S* = 0.75 and *S* = 5. As seen, the
311 Ha_{cr} is obtained as 0.372 for *S* = 0.75 and 2.061 for *S* = 5. The reason for the maximum flow rate
312 for each specific magnetic field intensity (Ha_{cr}) in the presence of lateral electric field, can be
313 found out by investigating added terms to the Navier-Stokes equation along the x direction (
314 $-\sigma E_z B_y \, \& \, -\sigma u B_y^2$). By enhancing the value of transverse magnetic field, when driving part (
315 $-\sigma E_z B_y$) is greater than deterrent part ($-\sigma u B_y^2$), source term leads to apply a force to fluid in the
316 same direction and flow rate augments. On the other hand, this velocity enhancement due to
317 increase in magnetic field is not stable because by incrementing velocity, deterrent part
318 augments, gradually. Finally, it could cause the deterrent part of this relation to become greater
319 than driving part and consequently, a force opposite of the flow direction is applied to the fluid
320 leading to a reduction in flow rate passing through the microchannel. For each value of *Ha* which
321 the source term of Eq. (10) becomes maximum (critical Hartmann number), maximum flow
322 velocity occurs.

323   While Figure 9 shows how Ha_{cr} in which the maximum flow rate and average velocity can
324 be obtained in each dimensionless parameter of lateral electric field (*S*), Figure 10 shows the
325 results of obtained Ha_{cr} and the maximum speed of flow versus *S*. Figure 10 .a indicates the
326 variations of Ha_{cr} as a function of dimensionless parameter of lateral electric field (*S*) influenced
327 by an axial electric field and pressure difference inside a 3-D microchannel with square a cross-
328 section. As seen, for values of *S* < 20, by increasing the dimensionless parameter of lateral
329 electric field, Ha_{cr} augments at a high rate. However, for the values of *S* > 20, the intensity of
330 Ha_{cr} decreases, gradually.

331   Figure 10 .b represents maximum dimensionless average velocity as a function of *S* under
332 influence of *α* and *Ω*. Maximum average flow velocity in the microchannel occurs at Ha_{cr}
333 corresponding to each *S*, which the value of Ha_{cr} versus *S* is presented in figure 10. a. By
334 increasing *S*, maximum average velocity in microchannel and resultant passing flow rate
335 enhances continually. The notable point is that in the constant axial electric field and the same
336 conditions, by adding a lateral electric field with much lower power than the axial electric field

9

337 and transverse magnetic field, the flow rate in the microchannel can be enhanced, and
338 electroosmotic flow can be amplified.

339 It should be mentioned that in Figure 10 .a and Figure 10 .b, for each value of *S*, there is a
340 corresponding symbol in both figures. For instance, in Figure 10 .b, at *S* = 20, $U_{m_{max}} = 2.2$, and
341 the corresponding Ha_{cr} value for this amount of *S* can be found in Figure 10 .a, which is around
342 3.7.

343   In Figure 11 .a Ha_{cr} as a function of *S* is drawn for 5 different values of *Ω*. As seen, by
344 increasing dimensionless parameter of pressure gradient (*Ω*) for each value of *S*, critical
345 Hartmann number (Ha_{cr}) reduces. The reason for this could be that the rise in pressure gradient
346 results in a reduction in the impact of the electroosmotic phenomenon on fluid motion in
347 comparison to the movement caused by the axial pressure gradient. Figure 11 .b presents the
348 variation of Ha_{cr} as a function of *Ω* for 3 lateral electric fields. By augmenting pressure
349 difference along the microchannel, Ha_{cr} tends to decrease. As seen, for *S* = 0.5, the value of
350 Ha_{cr} in *Ω* = 1 and *Ω* = 20 has a 44% difference, while the difference is about 7% for *S* = 50.
351 Therefore, the effect of *Ω* on Ha_{cr} decreases by increasing *S*.

352   Figure 12 indicates the effect of dimensionless parameter of lateral electric field (*S*) on the
353 Poiseuille number (*Po*) as a function of *Ha* for developed flow inside a microchannel with square
354 cross-section influenced by axial electric field. As seen, in general, by enhancing *Ha*, *Po*
355 augments. However, for different values of *S*, *Po* figure as the function of *Ha* shows a different
356 behavior. Thus, for *S* = 0 and *S* = 0.5, *Po* continually increases by enhancing *Ha*. In *S* = 0, flow
357 rate reduces by increasing *Ha*. Since, *Po* has reverse relation with the average velocity of flow
358 $\left(Po \propto \dfrac{1}{U_m} \right)$, reduction of average velocity of flow leads to augmentation of the value of *Po*. In *S*
359 = 0.5, Ha_{cr} has a negligible effect on the behavior of *Po* because of its small amounts
360 $\left(Ha_{cr} = 0.25 \right)$. For other electric fields' intensities, it has been seen that by increasing *Ha*, first
361 *Po* tends to decrease and then tends to increase. Indeed, minimum value of *Po* in each lateral
362 electric field, occurs approximately at the range of Ha_{cr} for that field. Because in this range,
363 average velocity of flow is maximum and according to reverse relation between average velocity
364 and *Po*, Poiseuille number decreases.

365   Figure 13 shows Ha_{cr} as a function of *S* in micro scale inside microchannel with the aspect
366 ratios of *a* = 2, 1, 0, 0.2, 0.5 with the same hydraulic diameter. The aspect ratio parameter is
367 defined as the ratio of height to the width of channel section $\left(a = \dfrac{H}{W} \right)$ [39]. As seen, by
368 converting square cross-section into two parallel plates (reduction of aspect ratio), the value of
369 Ha_{cr} enhances for each *S*. This change is more sensitive for low aspect ratios. By changing the
370 geometry of cross-section, because the hydraulic diameter is considered constant in each studied
371 state, the dimension of microchannel and the contact surface of wall and fluid change.

372 In the constant pressure gradient and lower aspect ratios, friction and dissipation due to the
373 contact of the fluid with the inner surface of the microchannel increase. This phenomenon is
374 because of the contact between fluid and the higher surface of microchannel's wall. Therefore,
375 the average velocity of flow passing through the microchannel reduces. By decreasing the flow
376 velocity, second term or negative part of $-\sigma E_z B_y - \sigma u B_y^2$ term reduces in Eq. (10). Consequently,
377 the stronger magnetic field or higher Ha is required to maximize flow rate or average velocity.

6-2   Heat transfer analysis

379 Figure 14 indicates dimensionless temperature profile of developed electroosmotic flow
380 influenced by lateral electric field and transverse magnetic field and pressure gradient. In the
381 absence of lateral electric field for the values of $Ha \le 1$, the enhancement of magnetic field leads
382 to a slight increase in maximum dimensionless temperature. However, for values of $Ha \ge 1$, the
383 augmentation of Hartmann number (Ha) causes considerable increment of maximum
384 dimensionless temperature profile and also, becomes wider. In the vicinity of surface in higher
385 Ha, the increase in temperature gradient means the enhancement of convective heat transfer
386 coefficient which means reduction in surface temperature difference and average temperature of
387 fluid, according to the constant heat flux condition on the surface.

388 Figure 15 shows dimensionless temperature profile of developed electroosmotic flow under
389 influence of various values of transverse magnetic field in the presence of lateral electric field. In
390 this figure flow velocity increased due to the interaction of driving and deterrent forces caused
391 by the electromagnetic field applied to the channel. Under influence of this condition, local
392 temperature of fluid reduces causing the augmentation of the value of $T - T_w$. Also, the increase
393 in average velocity leads to a reduction in average temperature in each cross-section. Therefore,
394 the value of $T_m - T_w$ increases in the denominator of the dimensionless temperature θ. However,
395 the increment of numerator of θ is lower than the increase in its denominator. Consequently, by
396 enhancing the value of Ha, the value of dimensionless temperature decreases in the cross-
397 section. By passing from Ha_{cr}, Hartmann number increment leads to decrease in the average
398 velocity of flow and heat transfer, because the movement of fluid mass reduces, and the value of
399 heat transfer diffusion rate enhances. Consequently, the value of dimensionless temperature
400 increases in the cross-section.

401 Figure 16 reveals the effect of lateral electric field on Nusselt number (Nu) in electroosmotic
402 developed flow for each Ha inside a microchannel with square cross-section influenced by
403 distinct lateral electric field (S) and pressure gradient. For $S = 0$ and $S = 0.5$, by increasing Ha,
404 Nu has incremental trend and enhances in all values of Ha. According to constant heat flux
405 boundary condition $\left(q'' = h\left(T_w - T_m\right)\right)$, Ha enhancement leads to reduction in $T_w - T_m$ and
406 consequently, increase in convective heat transfer coefficient, gradually. In the stronger lateral
407 electric field ($S \ge 5$), Nu becomes minimum in a specific Ha called critical Hartmann number
408 $\left(Ha_{cr,T}\right)$. By comparing around the Nusselt number minimization, it reveals that $Ha_{cr,T}$ is
409 greater than Ha_{cr} for $S = 5,10$ and is lower than Ha_{cr} for $S = 20,50$.

410

7　Conclusion

This research studied the electroosmotic flow of an electrolyte solution under the influence of a lateral electric field and a transverse magnetic field inside a microchannel. The purpose of this paper was to do a three-dimensional simulation which is necessary for practical applications, and to observe the flow physics and investigate the effect of different parameters on it. For modeling the electric potential in the electrolyte at the vicinity of walls, the Poisson-Boltzmann equation is used with the Debye-Hückel approximation. The governing equations of the flow are solved by using a numerical code and finite volume method by utilizing SIMPLEC algorithm. Also, the properties of the fluid are proposed constant.

Although effective parameters on flow are mainly implemented for microchannel with a square cross-section, the effect of the aspect ratio of channel cross-section is investigated on the microchannel flow. In addition, energy equation is solved by considering constant heat flux and Joule heating. The following conclusions are drawn from the results of this research:

- A secondary flow is created with a specific pattern at the microchannel cross-section due to simultaneous application of lateral electric field and transverse magnetic field on electroosmotic flow.
- By increasing the rate of the lateral electric field, the value of the critical Hartmann number enhances which flow rate becomes maximum. However, from a specific value of the lateral electric field, the enhancement rate of the critical Hartmann number decreases. In case of the lateral electric field parameter of $S = 0.5$, Ha_{cr} has 44% difference Between $\Omega = 1$ and $\Omega = 20$.
- The geometry of the microchannel cross-section affects the value of the critical Hartmann number. So that by changing aspect ratio from rectangular cross-section to squared, the value of Ha_{cr} augments, in this augmentation is more sensitive to lower aspect ratios.

In higher lateral electric fields, first, the gradual enhancement of magnetic field leads to reduced Nusselt number of development flow. However, after a specific value of the Hartmann number, the augmentation of the magnetic field leads to the enhancement of the Nusselt number. In the lower values of lateral electric fields, by increasing Hartmann number, Nusselt number enhances steadily. This flow and heat transfer problem can be employed in many areas such as bioengineering and is particularly useful in the manufacture of pharmaceutical microfluidic devices and flow delivery systems.

Nomenclature

b	Induced magnetic field, Vsm^{-2}
B	B Applied externally magnetic field strength, Vsm^{-2}
B_y	Applied magnetic field in y-direction, Vsm^{-2}
D_H	Hydraulic diameter, m
e	Charge of an electron, C
E	Externally Applied electric field strength, Vm^{-1}
E_x	Externally Applied electric field in x-direction, Vm^{-1}
E_z	Externally Applied electric field in z-direction, Vm^{-1}

F	Body force vector, N
F_{EK}	Electrokinetic body force, N
H	Microchannel half height, m
Ha	Hartmann number
Ha_{cr}	Critical Hartmann number
$Ha_{cr,T}$	Thermal critical Hartmann number
J	Induced electric current density, Am^{-1}
k_B	Boltzmann constant, JK^{-1}
L	Micro channel length, m
N	Ionic number concentration, m^{-3}
n_0	Bulk concentration of the ions, m^{-3}
P	Pressure, Nm^{-2}
Re_m	Magnetic Reynolds number
S	Dimensionless electric field in z-direction
T	Absolute temperature, K
u	Flow velocity in x-direction, ms^{-1}
U	Dimensionless flow velocity in x-direction
U_{av}	Dimensionless average flow velocity
u_{av}	Average flow velocity in x-direction, ms^{-1}
u_{HS}	Helmholtz-Smoluchowski velocity, ms^{-1}
u_{max}	Maximum flow velocity in x-direction, ms^{-1}
U_{max}	Dimensionless maximum flow velocity
v	Flow velocity in y-direction, ms^{-1}
V	Flow velocity vector, ms^{-1}
w	Flow velocity in z-direction, ms^{-1}
Y	Dimensionless height
z_i	Valency of i$^{\text{th}}$ ionic species
α	Dimensionless electric field in x-direction
ε	Relative permittivity of the medium
ε_0	Permittivity of free space, $CV^{-1}m^{-1}$
ς	Wall zeta potential, V
κ	Debye-Hückel parameter, m^{-1}
K	Dimensionless Debye-Hückel parameter
λ_D	Debye length, m
μ	Viscosity of the electrolyte, $kgm^{-1}s^{-1}$
ρ_e	Electric charge density, Cm^{-3}
ρ_f	Electrolyte density, kgm^{-3}
σ	Electric conductivity of the electrolyte, Sm^{-1}
ϕ	Electrostatic potential, V
ψ	Electrical double layer potential, V

Ω	Dimensionless pressure gradient

444

445

446 **References**

447 Gad-El-Hak, M., "The fluid mechanics of microdevices—the freeman scholar lecture", *Journal*
448 *of Fluids Engineering, Transactions of the ASME*, **121**(1), pp. 5–33 (1999).

449 Probstein, R. F., *Physicochemical Hydrodynamics: An Introduction*, John Wiley & Sons (2005).

450 Manz, A., Graber, N., and Widmer, H. M., "Miniaturized total chemical analysis systems: A
451 novel concept for chemical sensing", *Sens Actuators B Chem*, **1**(1–6), pp. 244–248 (1990).

452 Jang, J. and Lee, S. S., "Theoretical and experimental study of MHD (magnetohydrodynamic)
453 micropump", *Sens Actuators A Phys*, **80**(1), pp. 84–89 (2000).

454 Laser, D. J. and Santiago, J. G., "A review of micropumps", *Journal of Micromechanics and*
455 *Microengineering*, **14**(6), pp. R35–R64 (2004).

456 Nguyen, N. T., Huang, X., and Chuan, T. K., "MEMS-micropumps: A review", *Journal of*
457 *Fluids Engineering, Transactions of the ASME*, **124**(2), pp. 384–392 (2002).

458 Karniadakis, G., Beskok, A., and Aluru, N., *Microflows and Nanoflows: Fundamentals and*
459 *Simulation*, Springer Science & Business Media (2006).

460 Das, S., Chakraborty, S., and Mitra, S. K., "Magnetohydrodynamics in narrow fluidic channels
461 in presence of spatially non-uniform magnetic fields: Framework for combined
462 magnetohydrodynamic and magnetophoretic particle transport", *Microfluid Nanofluidics*, **13**(5),
463 pp. 799–807 (2012).

464 Sarkar, S., Ganguly, S., and Dutta, P., "Thermofluidic characteristics of combined electroosmotic
465 and pressure driven flows in narrow confinements in presence of spatially non-uniform magnetic
466 field", *Int J Heat Mass Transf*, **104**, pp. 1325–1340 (2017).

467 Wang, P. J., Chang, C. Y., and Chang, M. L., "Simulation of two-dimensional fully developed
468 laminar flow for a magneto-hydrodynamic (MHD) pump", *Biosens Bioelectron*, pp. 115–121
469 (2004).

470 Chakraborty, S. and Paul, D., "Microchannel flow control through a combined
471 electromagnetohydrodynamic transport", *J Phys D Appl Phys*, **39**, p. 5364 (2006).

472 Duwairi, H. and Abdullah, M., "Thermal and flow analysis of a magneto-hydrodynamic
473 micropump", *Microsystem Technologies*, **13**(1), pp. 33–39 (2007).

474 Chakraborty, R., Dey, R., and Chakraborty, S., "Thermal characteristics of
475 electromagnetohydrodynamic flows in narrow channels with viscous dissipation and Joule
476 heating under constant wall heat flux", *Int J Heat Mass Transf*, **67**, pp. 1151–1162 (2013).

477 Escandón, J., Santiago, F., Bautista, O., and Méndez, F., "Hydrodynamics and thermal analysis
478 of a mixed electromagnetohydrodynamic- pressure driven flow for Phan-Thien-Tanner fluids in
479 a microchannel", *International Journal of Thermal Sciences*, **86**, pp. 246–257 (2014).

14

480. Kiyasatfar, M. and Pourmahmoud, N., "Laminar MHD flow and heat transfer of power-law fluids in square microchannels", *International Journal of Thermal Sciences*, **99**, pp. 26–35 (2016).

483. Wang, L., Jian, Y., Liu, Q., Li, F., and Chang, L., "Electromagnetohydrodynamic flow and heat transfer of third grade fluids between two micro-parallel plates", *Colloids Surf A Physicochem Eng Asp*, **494**(494), pp. 87–94 (2016).

486. Qi, C. and Wu, C., "Electromagnetohydrodynamic flow in a rectangular microchannel", *Sens Actuators B Chem*, **263**, pp. 643–660 (2018).

488. Yang, C., Jian, Y., Xie, Z., and Li, F., "Heat transfer characteristics of magnetohydrodynamic electroosmotic flow in a rectangular microchannel", *European Journal of Mechanics-B/Fluids*, **74**, pp. 180–190 (2019).

491. Moradmand, A., Saghafian, M., and Mofrad, B., "Electroosmotic Pressure-Driven Flow through a Slit Micro-Channel with Electric and Magnetic Transverse Field", *Journal of Applied Fluid Mechanics*, **12**, pp. 961–969 (2019).

494. Yang, C.-H. and Jian, Y.-J, "Effect of patterned hydrodynamic slip on electromagnetohydrodynamic flow in parallel plate microchannel", *Chinese Physics B*, **29**(11), p. 114101 (2020).

497. Deng, S., Xiao, T., and Wu, S., "Two-layer combined electroosmotic and pressure-driven flow of power-law fluids in a circular microcapillary", *Colloids Surf A Physicochem Eng Asp*, **610**, p. 125727 (2021).

500. Ge, Y., He, Q., Lin, Y., Yuan, W., Chen, J., and Huang, S.-M., "Multi-objective optimization of a mini-channel heat sink with non-uniform fins using genetic algorithm in coupling with CFD models", *Appl Therm Eng*, **207**, p. 118127 (2022).

503. Wang, G., Qian, N., and Ding, G., "Heat transfer enhancement in microchannel heat sink with bidirectional rib", *Int J Heat Mass Transf*, **136**, pp. 597–609 (2019).

505. Biswas, N., Mondal, M. K., Mandal, D. K., Manna, N. K., Gorla, R. S. R., and Chamkha, A. J., "A narrative loom of hybrid nanofluid-filled wavy walled tilted porous enclosure imposing a partially active magnetic field", *Int J Mech Sci*, **217**, p. 107028 (2022).

508. Mandal, D. K., Biswas, N., Manna, N. K., Gayen, D. K., Gorla, R. S. R., and Chamkha, A. J., "Thermo-fluidic transport process in a novel M-shaped cavity packed with non-Darcian porous medium and hybrid nanofluid: Application of artificial neural network (ANN)", *Physics of Fluids*, **34**(3), p. 033608 (2022).

512. Datta, A., Debbarma, D., Biswas, N., Sanyal, D., and Das, A. K., "The Role of Flow Structures on the Thermal Performance of Microchannels With Wall Features", *J Therm Sci Eng Appl*, **13**(2) (2020).

515. Amit, K., Datta, A., Biswas, N., Das, S., and Das, P., "Designing of microsink to maximize the thermal performance and minimize the Entropy generation with the role of flow structures", *Int J Heat Mass Transf*, **176**, p. 121421 (2021).

15

18. Biswas, N., Chamkha, A. J., and Manna, N. K., "Energy-saving method of heat transfer enhancement during magneto-thermal convection in typical thermal cavities adopting aspiration", *SN Appl Sci*, **2**(11), p. 1911 (2020).

19. Alharbi, K. A. M., Khan, Z., Zuhra, S., Islam, S., Ali, A., Tag-Eldin, E., and Mahmoud, S. R., "Numerical Study of the Electromagnetohydrodynamic Bioconvection Flow of Micropolar Nanofluid through a Stretching Sheet with Thermal Radiation and Stratification", *ACS Omega*, **7**(47), pp. 42733–42751 (2022).

20. Ciocanel, C. and Islam, N., "Integrated Electro-Magnetochydrodynamic Micropumps and Methods for Pumping Fluids ", U.S. patent US-8480377-B2 (July 9, 2013).

21. Alipanah, M., Hafttananian, M., Hedayati, N., Ramiar, A., and Alipanah, M., "Microfluidic on-demand particle separation using induced charged electroosmotic flow and magnetic field", *J Magn Magn Mater*, **537**, p. 168156 (2021).

22. Masliyah, J. H. and Bhattacharjee, S., *Electrokinetic and Colloid Transport Phenomena*, Wiley-Interscience (2006).

23. Davidson, P. A., "An introduction to magnetohydrodynamics" (2002).

24. Müller, U. and Bühler, L., *Magnetofluiddynamics in Channels and Containers*, Springer Berlin Heidelberg, Berlin, Heidelberg (2001).

25. Mirbozorgi, S. A., Niazmand, H., and Renksizbulut, M., "Electro-osmotic flow in reservoir-connected flat microchannel with non-uniform zeta potential", *Journal of Fluids Engineering, Transactions of the ASME*, **128**(6), pp. 1133–1143 (2006).

26. Deng, S. Y., Jian, Y. J., Bi, Y. H., Chang, L., Wang, H. J., and Liu, Q. S., "Unsteady electroosmotic flow of power-law fluid in a rectangular microchannel", *Mech Res Commun*, **39**(1), pp. 9–14 (2012).

27. Lim, J., Lanni, C., Evarts, E. R., Lanni, F., Tilton, R. D., and Majetich, S. A., "Magnetophoresis of nanoparticles", *ACS Nano*, **5**(1), pp. 217–226 (2011).

28. Nguyen, N.-T., "Micro-magnetofluidics: interactions between magnetism and fluid flow on the microscale", *Microfluid Nanofluidics*, **12**(1–4), pp. 1–16 (2012).

29. Chen, X. and Hu, Z., "Study aspect ratio of microchannel on different polymer substrates with CO2 laser and hot bonding for microfluidic chip", *AIP Adv*, **8**(1), p. 015116 (2018).

List of Captions

- **Tables**

551   Table 1. Boundary conditions of the problem

552   Table 2. Dimensionless parameters for implementing the results.

553   Table 3. The percentage change for dimensionless temperature and Poiseuille number at α = 2256, K = 20 and Ω = 1

554   • **Figures**

555   Figure 1 . The geometry of microchannel

556   Figure 2 . Dimensionless electric potential distribution in microchannel cross-section at ζ = -25mV and K = 32

557   Figure 3. Velocity distribution under influence of Ha = 2

558   Figure 4 . Velocity distribution diagram in square microchannel cross-section under influence of E_x =10000 V / m in two values
559   of K = 20 and K = 100

560   Figure 5 . Velocity distribution in 2D microchannel cross-section under influence of α = 2256, S = 50, K = 4, and Ω = 1.

561   Figure 6 . Velocity profile in microchannel with square cross-section under influence of α = 2256, Z = 0, K = 20, and Ω = 1 at
562   different Hartmann numbers

563   Figure 7- Streamlines of fluid flow in microchannel cross-section under influence of S = 5, Ha = 0.5, α = 2256, K = 20, and Ω =
564   1 on velocity contour a. V component, b. W component

565   Figure 8 - Developed velocity in microchannel cross- section under influence of S = 5, α = 2256, and Ω = 1, a. $Ha \leq 1$, b. $Ha \geq 1$

566   Figure 9 - Average velocity variations with Hartmann number under influence of α = 2256, K = 20, and Ω = 1 for a. S = 0.75 , b.
567   S = 5

568   Figure 10 - a. Critical Hartmann number, b. dimensionless maximum average velocity by means of dimensionless lateral electric
569   field in 3D microchannel with square cross-section under influence of α = 2256, K = 20, and Ω = 1

570   Figure 11 - Critical Hartmann, number, a. by means of dimensionless lateral electric field under influence of α = 2256, and K =
571   20 in different values of Ω, b. by means of dimensionless pressure gradient under influence of α = 2256, and K = 20 in different
572   values of S, in 3D microchannel with square cross-section

573   Figure 12 . Effect of lateral electric field on graph of Poiseuille number by means of Ha under influence of α = 2256, K = 20, and
574   Ω = 1

575   Figure 13 . Critical Hartmann number by means of dimensionless lateral electric field under influence of α = 2256, K = 20, and Ω
576   = 1 in different values of aspect ratio

577   Figure 14 . Fully developed and dimensionless temperature profile in microchannel with square cross-section on Z = 0 line
578   without applying lateral electric field

579   Figure 15 . Fully developed and dimensionless temperature distribution in microchannel with square cross-section on Z = 0 line
580   in presence of lateral electric field

581   Figure 16 . Effect of applying lateral electric field on Nusselt number figure by means of Hartmann number under influence of α
582   = 2256, K = 20, and Ω = 1

583

584   **List of tables and figures**

585   • **Tables**

586　Table 1

Inlet	Wall	Outlet
$u = u_{in}$	$u = 0$	zero gradient in the direction perpendicular to outlet section
$v = 0$	$v = 0$	zero gradient in the direction perpendicular to outlet section
$w = 0$	$q'' = -k\dfrac{\partial T}{\partial n}$	zero gradient in the direction perpendicular to outlet section
$T = T_{in}$	$\psi = \zeta$	zero gradient in the direction perpendicular to outlet section

587

588　Table 2

Dimensionless Length	$(X,Y,Z) = \left(\dfrac{x}{D_H}, \dfrac{y}{H}, \dfrac{z}{W}\right)$	Dimensionless velocity	$(U,V,W) = \left(\dfrac{u}{U_{HS}}, \dfrac{v}{U_{HS}}, \dfrac{w}{U_{HS}}\right)$
Dimensionless average velocity	$U_m = \dfrac{u_m}{U_{HS}}$	Dimensionless temperature	$\theta = \dfrac{T - T_w}{T_m - T_w}$
Nusselt number	$Nu = \dfrac{hD_H}{k}$	Hartman number	$Ha = BD_H\sqrt{\dfrac{\sigma}{\mu}}$
Debye-Huckle parameter	$K = \kappa D_H = \sqrt{\dfrac{2e^2 z^2 n_0}{\varepsilon\varepsilon_0 k_B T}}\,D_H$	Dimensionless axial electric field	$\alpha = \dfrac{E_x L}{\zeta}$
Dimensionless lateral electric field	$S = \dfrac{E_z D_H}{U_{HS}}\sqrt{\dfrac{\sigma}{\mu}}$	Dimensionless pressure gradient along the channel	$\Omega = \dfrac{\Delta P D_H^2}{\mu L U_{HS}}$
Dimensionless electric potential	$\Psi = \dfrac{ze\psi}{k_B T}$	Poiseuille number	$Po = C_f\,Re$
Reynolds number	$Re = \dfrac{\rho_f u_m D_H}{\mu}$		

589

590

591　Table 3

a = 0.5 S = 0.25, Ha = 0.25			a = 1 S = 1, Ha = 0.5		
Grid	Percentage	Percentage	Grid	Percentage	Percentage

18

	change of Po	change of θ		change of Po	change of θ
20×32×75	1.53	0.4	20×20×50	2.434	0.896
40×64×100	0.23	0.13	40×40×100	0.326	0.896
80×128×150	-	-	80×80×200	-	-

a = 0 S = 5, Ha = 0.5			a = 0.2 S = 0.5, Ha = 0.5		
Grid	Percentage change of Po	Percentage change of θ	Grid	Percentage change of Po	Percentage change of θ
20×50	2.536	1.071	16×20×75	2.297	0.896
40×100	0.156	0.587	32×80×100	0.452	0.242
80×200	-	-	64×160×150	-	-
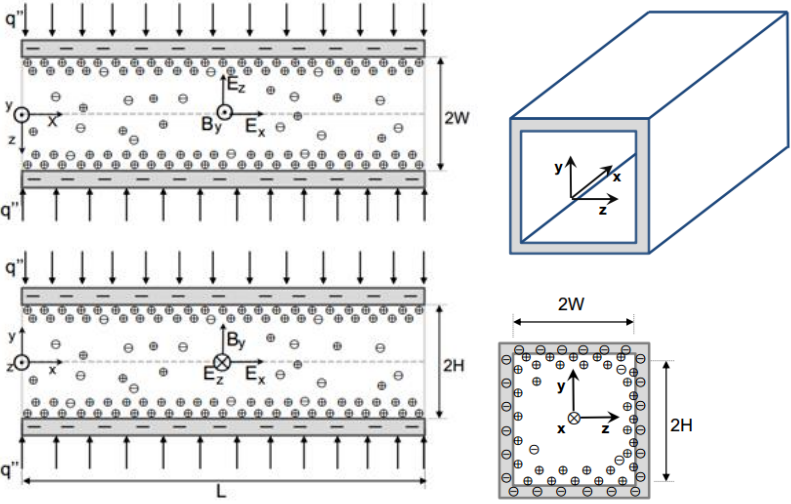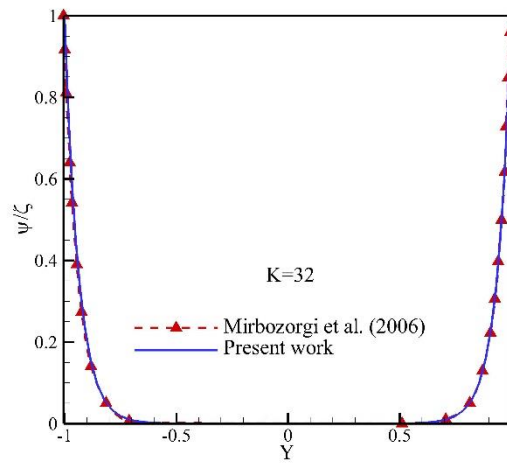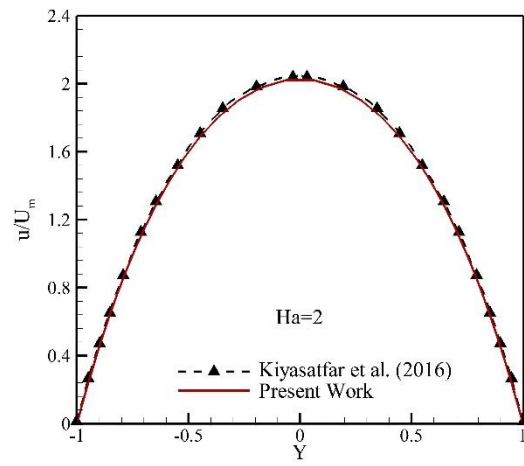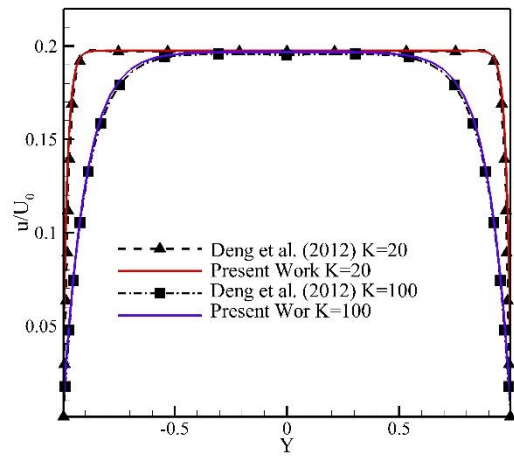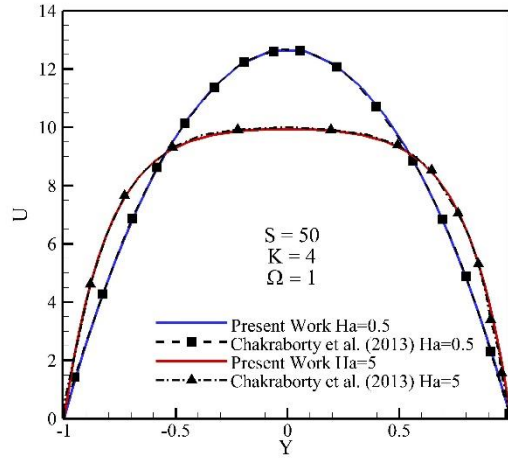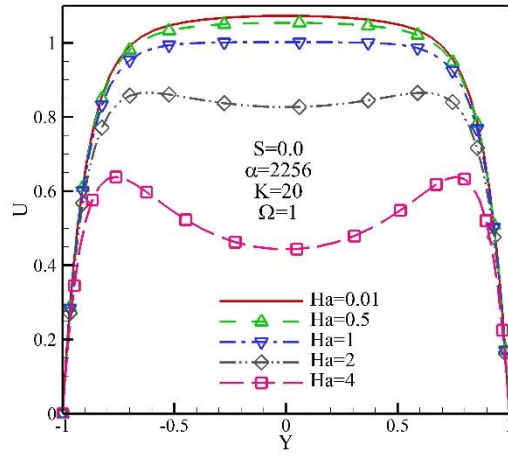
- **Figures**

Figure 1

596

597   Figure 2

598

Figure 3

599

600   Figure 4

21

Figure 5

601

602   Figure 6

603

604

22

(a)

(b)

Figure 7

(a)

(b)

Figure 8

605

23

Figure 9

Figure 10

24

(a)   (b)

Figure 11

606

(a)   (b)
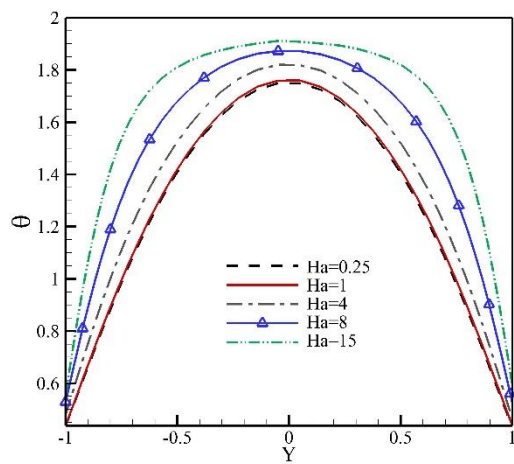
25

607

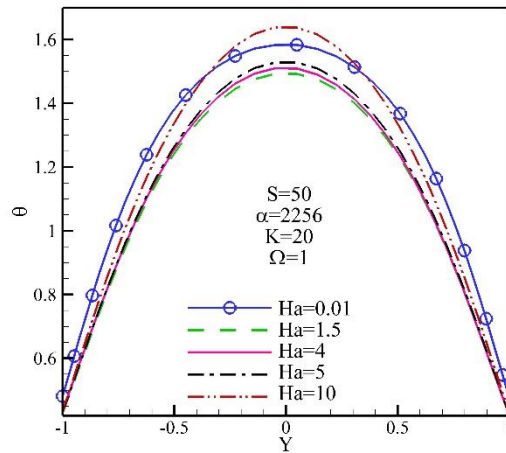Figure 12

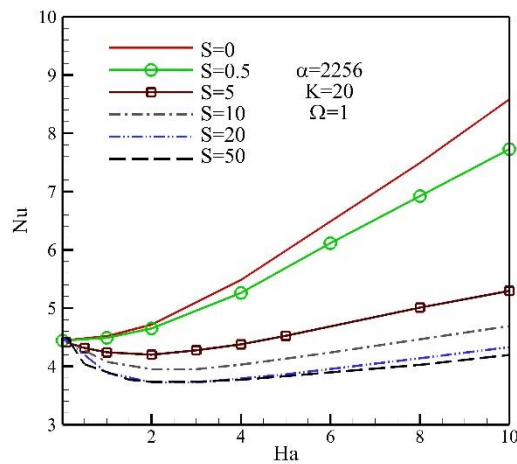Figure 13

609

610

Figure 14

26
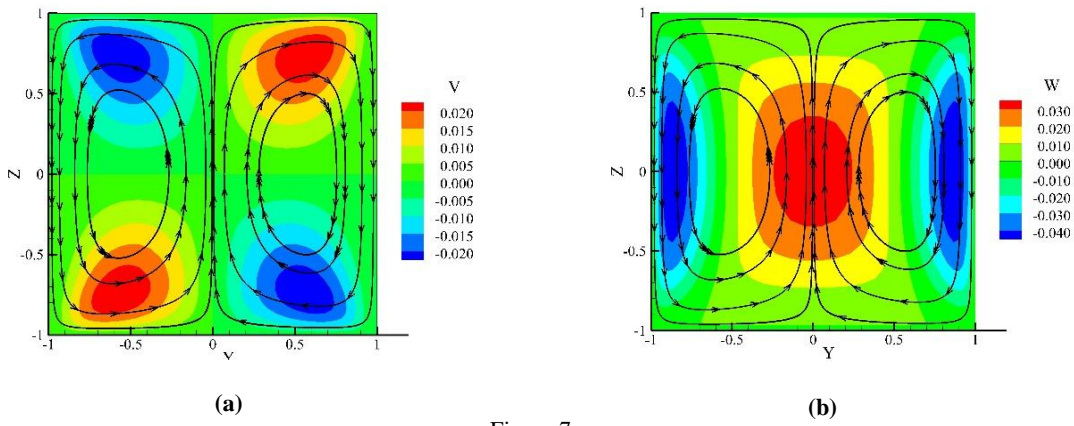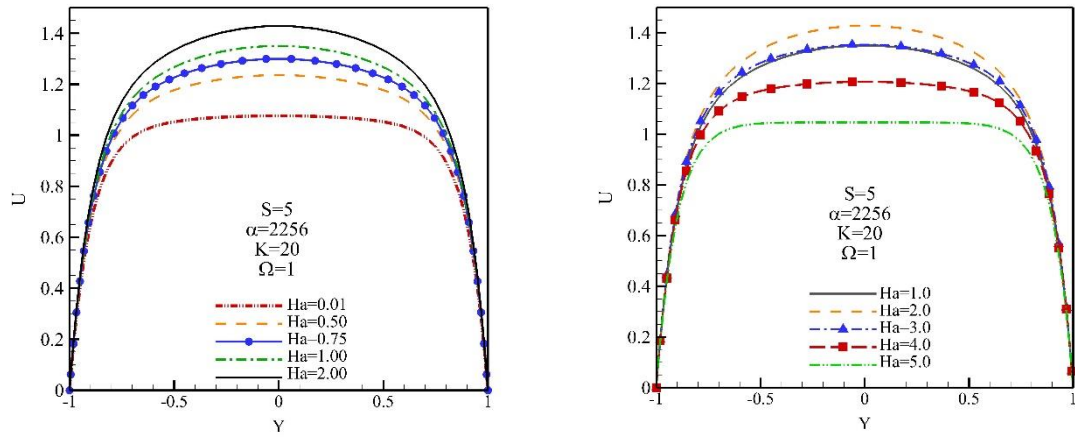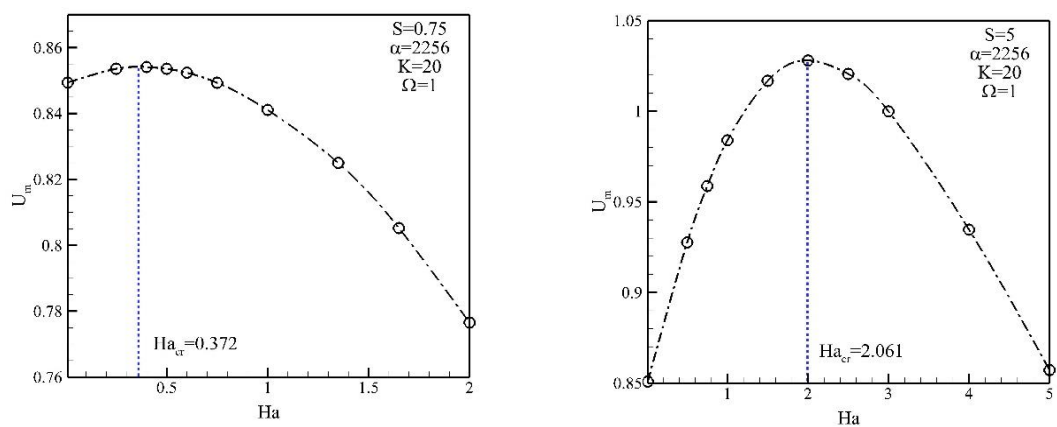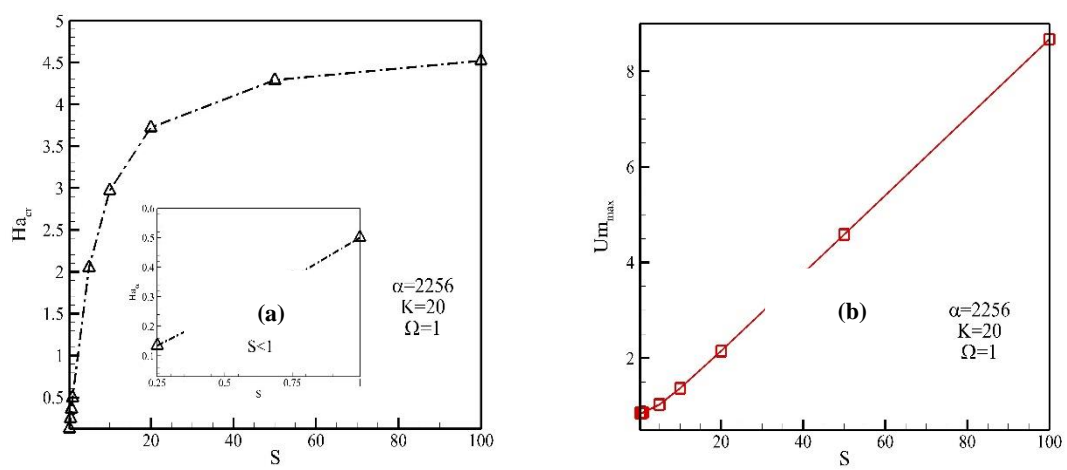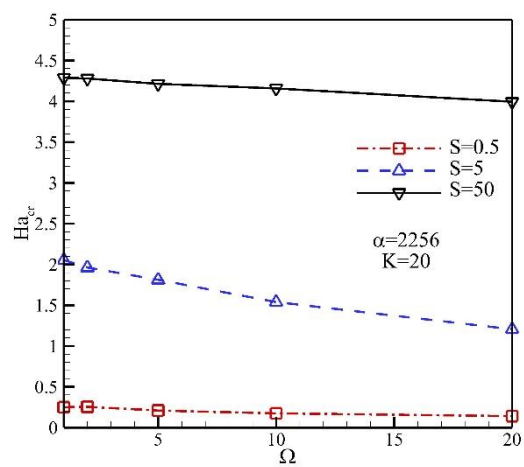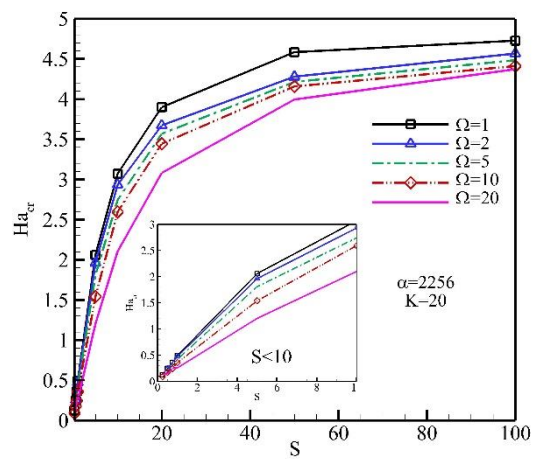
Figure 15

Figure 16

Biographies

Dr. Mohsen Saghafian is an Associate Professor in the Department of Mechanical Engineering at Isfahan University of Technology, Iran, specializing in CFD, Fluid Mechanics, Heat and Mass Transfer, MHD, EHD, Microfluidics, Numerical techniques, and Turbulence. His research focuses on various topics, such as particle separation in microfluidic devices, acoustic radiation force on biological cells, blood flow in stenosed arteries, tumor modeling, fluid flow and heat transfer in microchannels under electric and magnetic fields, and convection heat transfer in nonhomogeneous nanofluids.

Hossein Seyedzadeh received his M.Sc. degree in Mechanical Engineering from Isfahan University of Technology, Isfahan, Iran, in 2020. He is now a PhD student and research assistant

27

626 in the department of Civil Engineering at Stony Brook University, NY, USA. His research
627 interests are CFD simulation of Energy, Environmental & Biological Fluid Dynamics. He is also
628 experienced in the MHD and EHD flows.

629

630 **Abolfazl Moradmand** received his B.Sc. degree in mechanical engineering from Yazd
631 University, Yazd, Iran, in 2014 and his M.Sc. degree in mechanical engineering from Isfahan
632 University of Technology, Isfahan, Iran, in 2018. His research interests include Electro-
633 Hydrodynamic flows and Microchannels.

634